Invited Articles

Methods for studying Tan's contact in the BCS-BEC crossover

Manuel Jäger and Johannes Hecker Denschlag
Institut für Quantenmaterie and Center for Integrated Quantum Science and Technology (IQST), Universität Ulm, Albert-Einstein-Allee 45, 89081 Ulm, Germany

(Received 6 May 2024; accepted 20 May 2024; published 25 June 2024)

In a parallel publication [Phys. Rev. Lett. **132**, 263401 (2024)] we demonstrate that photoinduced two-body loss can be used to measure Tan's contact with high precision in a two-component Fermi gas. Here, in the present companion paper, we provide relevant background information on this work and describe in detail the methodology for both the experiments and the data analysis. We first review various theoretical approaches for calculating the contact and identify areas in phase space of the spin-balanced Fermi gas where Tan's contact has not yet been determined. Next, we provide detailed information on our experimental methods, in particular, explaining the measurement and calibration procedures to achieve a high-precision results for the contact. Afterwards, we study the variation of the decay laws of two-body loss in a Fermi gas in the crossover from the Bardeen-Cooper-Schrieffer (BCS) to the Bose-Einstein-condensate (BEC) regime, verifying previous predictions. Finally, we determine the closed-channel fraction of the Fermi gas and compare it to previous measurements and theoretical calculations.

DOI: 10.1103/PhysRevA.109.063330

I. INTRODUCTION

Tan's contact, first introduced by Tan in 2008 [1–3], is a measure for short-range two-body correlations and quantifies the likelihood of finding two interacting fermions at very small distance. It is an important quantity for describing strongly interacting Fermi gases [1–5]. Tan's contact has been investigated both experimentally and theoretically in various approaches [6–16]. One experimental approach to measure Tan's contact is by studying two-body loss in the gas, where the loss is laser-induced. This was theoretically discussed in Refs. [16,17] and demonstrated by us in recent work [18]. Using this method we measured the contact across the entire phase diagram of the BCS-BEC crossover, thus providing a comprehensive picture of the pair correlations. We found that the method is quite convenient and allows for high-precision measurements.

Within the present companion paper, we provide additional background information on this work. In particular, we give a rough overview over previous work related to the contact in the BCS-BEC crossover, mapping out the so-far charted and uncharted phase space regions of the BCS-BEC crossover with respect to the contact. Furthermore, we lay out the experimental methods which allow for contact measurements at high precision. In addition, we discuss previous work on the closed-channel fraction of a Fermi gas which is closely related to the contact. Finally, we provide details on our experimental investigation on the decay laws of the photoinduced loss of atoms. As predicted by the authors of Ref. [16] and experimentally shown by the authors of Ref. [19] we confirm that the power law of the decay varies across the BCS-BEC crossover.

II. CHARTED AND UNCHARTED REGIONS OF TAN'S CONTACT IN THE BCS-BEC CROSSOVER

In the following we consider the phase space of the BCS-BEC crossover for a spin-balanced two-component Fermi gas with contact interactions which is trapped in a harmonic potential [20–22]. Such a Fermi gas has essentially only two degrees of freedom. (1) The coupling strength $(k_F a_s)^{-1}$, where k_F is the Fermi wave number and a_s is the s-wave scattering length. (2) The normalized temperature T/T_F where T_F is the Fermi temperature. Figure 1 shows the core of the BCS-BEC crossover phase space, in which the nature of the Fermi gas and its pair correlations fundamentally change. Below the critical temperature T_c (continuous line) superfluidity sets in. Here, one distinguishes three limiting regimes [20,21]. For $(k_F a_s)^{-1} \approx 0$ we have resonant superfluidity. For $(k_F a_s)^{-1} \gg 1$ we have the regime of Bose-Einstein condensation (BEC) of molecules. Finally, for $(k_F a_s)^{-1} \ll -1$ we have the regime of Bardeen-Cooper-Schrieffer (BCS) superfluid of atom pairs. For $T \gg T_c$ the gas is in the normal state. For the BEC and BCS regimes at $T = 0$ there are analytical ground-state energy expansions which can be used to describe properties of the gas for coupling strengths down to $|(k_F a_s)^{-1}| \approx 1$, see Fig. 1. For $T \gtrsim 0.5 T_F$ the gas properties of the harmonically trapped Fermi gas can be described in the framework of the quantum virial expansion [23]. At unitarity [i.e., $(k_F a_s)^{-1} = 0$] the scattering length a_s drops out of the description and therefore simplifies the problem. A variety of numerical calculations (e.g., the authors of Refs. [24–26] provided predictions for the gas properties and its contact for this regime. Furthermore, experimental investigations measured the equation of state (EOS) at $T \sim 0$ [27] filling the theoretical gap for $|(k_F a_s)^{-1}| \lesssim 1$. In addition, measurements were carried out at unitarity, determining, among other things, the contact [7–10,28].

Figure 1 shows that there are still large uncharted areas in phase space, especially for a strongly interacting gas close to unitarity at low temperature. Filling this area with precise data for the contact, was one of the main motivations for our work. To verify that our measurements of the contact (of a harmonically trapped Fermi gas) are consistent with previous

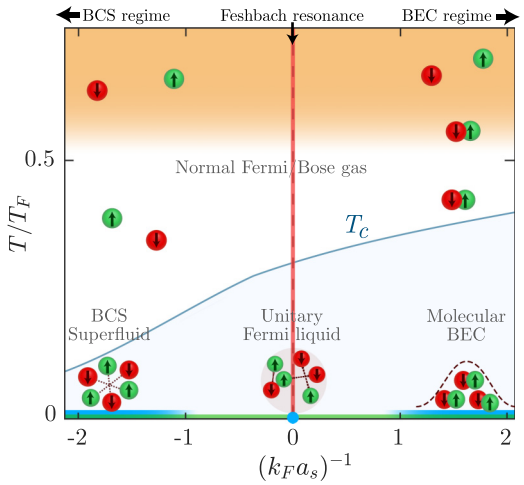

FIG. 1. Phase diagram of a spin-balanced Fermi gas in the BCS-BEC crossover. The green and red circles represent fermions of the two spin components and illustrate the different phases present in the crossover (see text). The thin blue-gray line marks the critical temperature for superfluidity T_C for a harmonically trapped Fermi gas, taken from Ref. [43]. In selected regions, the contact has been studied intensely theoretically and experimentally. For example, at zero temperature in the regions where $(k_F a_s)^{-1} < 1$, $= 0$, and >1 (thick blue lines and blue dot), the contact can be calculated from the BCS-, unitarity, and BEC ground-state energy expansions. In the orange marked area above $T/T_F \approx 0.5$, the quantum virial expansion is expected to start providing accurate results for a harmonically trapped Fermi gas [13]. For both the $T = 0$ (green broad line) and $(k_F a_s)^{-1} = 0$ (red broad line) regions, there are numerous theoretical and experimental studies for the contact (see text).

measurements by other groups and established theoretical descriptions of the gas we carried out comparisons. For this, the contact had to be extracted from several of these works and partially recalculated for our situation of a harmonically trapped Fermi gas. In the following we explain in detail how this was achieved.

The general approach is that we start out with an expression for the total energy E of a homogeneous Fermi gas in a volume V. Here, E is the total energy of the system including kinetic energy and interaction energy. We then make use of the relation [2]

$$\frac{dE}{d(1/a_s)} = -\frac{\hbar^2}{4\pi m} CV \tag{1}$$

that connects the homogeneous contact density C to the derivative of total systems energy E with respect to the s-wave scattering length a_s. This relation in general holds for a two-component Fermi gas at any temperature.

Next we use this C to calculate the total contact $\mathcal{I}$ of a harmonically trapped Fermi gas. In a harmonic trapping potential, the atom density is position dependent and thus the contact changes locally. In the spirit of the local density approximation (LDA), the total contact of the system $\mathcal{I}$ is then obtained by integrating $C(\vec{r})$ over the trap volume $\mathcal{I} = \int d^3r\, C(\vec{r})$. For this we follow the approach discussed in Appendix C of Ref. [16].

A. Tan's contact from the ground-state energy expansions

In this section, we closely follow the derivation of Tan's contact from the ground-state energy expansions as laid out in Ref. [16]. Only for the binding energy of molecule, we use a slightly improved expression.

At zero temperature T the total energy E is known analytically at various regions of the BCS-BEC crossover. For a homogeneous Fermi gas in the BCS limit the energy per volume V at zero temperature is given by the expansion

$$E/V = \frac{3}{5}\frac{\hbar^2\left(k_F^{\mathrm{hom}}\right)^2}{2m} n \times \left(1 + \frac{10}{9\pi} k_F^{\mathrm{hom}} a_s + 0.1855\left(k_F^{\mathrm{hom}} a_s\right)^2 + \cdots\right), \tag{2}$$

where n is the atom density and $k_F^{\mathrm{hom}} = (3\pi^2 n)^{1/3}$ is the Fermi momentum of the homogeneous gas [16,29,30]. The first three terms are the energy of the noninteracting Fermi gas, the Hartree-Fock mean-field correction, and the (fermionic) Lee-Huang-Yang correction, respectively.

Using relation (1) we obtain the contact density [2]

$$C = \mathcal{I}/V = 4\pi^2 n^2 a_s^2\left(1 + 1.049 k_F^{\mathrm{hom}} a_s + 0.2584\left(k_F^{\mathrm{hom}} a_s\right)^2 + \cdots\right). \tag{3}$$

At unitarity, the ground-state energy density is

$$E/V = \frac{3}{5}\frac{\hbar^2\left(k_F^{\mathrm{hom}}\right)^2}{2m} n\left(\xi + \frac{\zeta}{k_F^{\mathrm{hom}} a_s} + \cdots\right), \tag{4}$$

where $\xi \approx 0.367$ [31] is the Bertsch parameter and the constant $\zeta \approx 0.8$ [8]. Therefore, the contact density is

$$C = \frac{6\pi k_F \zeta}{5} n + \cdots. \tag{5}$$

In the BEC limit of tightly bound dimers the energy density at zero temperature can be approximated by

$$E/V = -n_d \frac{\hbar^2}{m a_s^2} + \frac{2\pi\hbar^2 a_{dd}}{2m} n_d^2\left(1 + 4.81\sqrt{n_d a_{dd}^3} + \cdots\right), \tag{6}$$

where the first term arises from the molecular binding energy for $a_s \to \infty$ and the next two terms from the mean field and the (bosonic) Lee-Huang-Yang correction, respectively [16]. Here, $n_d = n/2$ is the dimer density and $a_{dd} = 0.6\, a_s$ is the dimer-dimer scattering length [32]. The contact density becomes

$$C = \frac{4\pi n}{a_s} + 0.6\pi^2 n^2 a_s^2 (1 + 12.03\sqrt{n_d a_{dd}^3} + \cdots). \tag{7}$$

The homogeneous contact densities calculated from Eqs. (3), (5), and (7) are shown in Fig. 2.

Note that, for finite scattering lengths a_s, the expression for the binding energy per molecule

$$\frac{\hbar^2}{m a_s^2},$$

in Eq. (6) has to be modified by higher-order corrections [33,34]. At a coupling of $(k_F^{\mathrm{hom}} a_s)^{-1} = 1\,(2)$ these result in

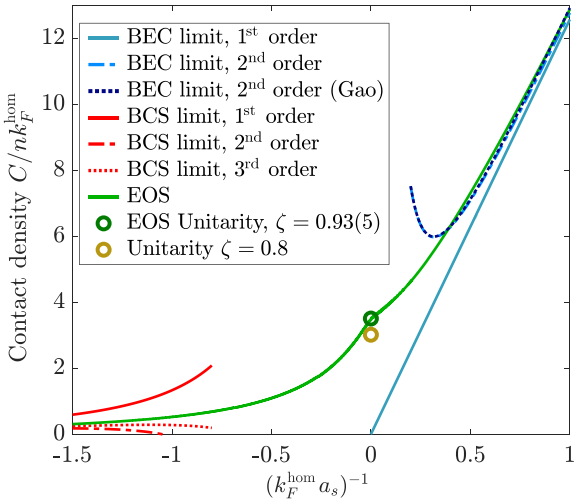

FIG. 2. Normalized contact density of a homogeneous system calculated from the ground-state energy expansions [Eqs. (3), (5), and (7)] and the equation of state (EOS) measurements. Also shown is the contact in the BEC limit with the binding energy correction for small a_s [34]. The different orders refer to the number of orders in Eqs. (3) and (7).

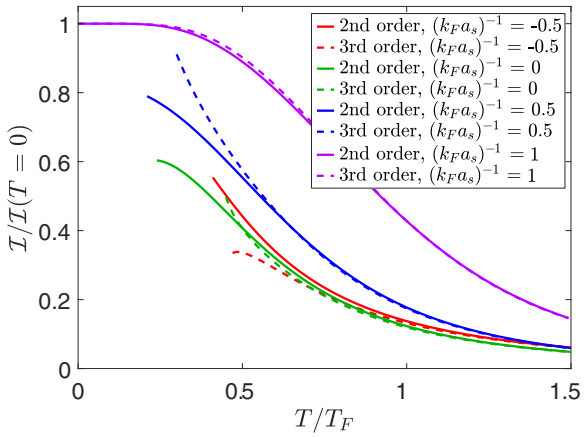

FIG. 3. Contact $\mathcal{I}$ of a harmonically trapped Fermi gas, as calculated with the second and third-order virial expansions for couplings $(k_Fa_s)^{-1} = (-0.5, 0, 0.5, 1)$. We normalize each contact curve $\mathcal{I}(T/T_F)$ with the respective zero-temperature value $\mathcal{I}(0)$, taken from our interpolation of the zero-temperature measurement, as shown in Fig. 2 of Ref. [18].

corrections of 1.4% (2.9%) towards a larger contact density, as shown in Fig. 2.

B. Tan's contact from the EOS measurements

Navon *et al.* carried out measurements of the equation of state (EOS) of a zero-temperature Fermi gas in the BCS-BEC crossover [27]. Here, we briefly explain the procedure to first obtain the contact density C and then the trap-integrated total contact $\mathcal{I}$ based on these measurements. The resulting curves are shown in Fig. 2 and Fig. 2 of Ref. [18]. In general, the total energy of a Fermi gas at zero temperature can be expressed as

$$E/V = \frac{3}{5}\frac{\hbar^2\left(k_F^{\rm hom}\right)^2}{2m} n\,\xi(\delta) - \Theta(a_s)\frac{n}{2}\frac{\hbar^2}{ma_s^2}, \tag{8}$$

where $\xi(\delta)$ can be viewed as a generalized Bertsch parameter relating the systems total energy to the Fermi energy at a given interaction parameter δ. Θ is the Heaviside step function and accounts for the existence of the Feshbach bound state with binding energy $\hbar^2/ma_s^2$ for $a_s > 0$. In the Supplementary Material of Ref. [27] the function $\xi(\delta)$ is defined as

$$\xi(\delta) = \frac{h(\delta) - \frac{\delta}{3}h'(\delta)}{\left(h(\delta) - \frac{\delta}{5}h'(\delta)\right)^{5/3}}. \tag{9}$$

Here, δ is related to the coupling parameter $(k_F^{\rm hom}a_s)^{-1}$ through an implicit equation

$$\left(k_F^{\rm hom}a_s\right)^{-1}(\delta) = \frac{\delta}{\left[h(\delta) - \frac{\delta}{5}h'(\delta)\right]^{1/3}}, \tag{10}$$

which can be solved numerically.

For the function $h(\delta)$, Padé approximations were given for both the BEC ($a_s > 0$) and BCS ($a_s < 0$) regime. The approximations, whose parameters were deduced from the EOS measurements, were made such that $h(\delta)$ is continuous at unitarity $(k_F^{\rm hom}a_s)^{-1} = 0$. The function $h'(\delta)$ denotes the derivative of $h(\delta)$. By combining Eqs. (8), (9), and (10) we find the systems energy E as a function of $(k_F^{\rm hom}a_s)^{-1}$. From this, the contact density C across the BCS-BEC crossover can be determined as in the previous section. The resulting curve is shown in Fig. 2.

We then integrate over the trap volume as described in Appendix C of Ref. [16] to get the total contact $\mathcal{I}$ for the harmonically trapped Fermi gas. Note that, although the Pad approximations for $h(\delta)$ are continuous at unitarity, they are not continuously differentiable there. As a result, both the calculated contact density and the total contact exhibit a kink there (see Fig. 2 and Fig. 2 of Ref. [18]).

C. Tan's contact within the quantum virial expansion

The quantum virial expansion has shown to be a powerful tool for investigating strongly interacting Fermi gases at high temperatures T [23]. In the high-temperature limit, the chemical potential μ of a Fermi gas approaches $-\infty$. Therefore, the fugacity $z = \exp(\mu/k_BT)$ becomes a small parameter, even for strong interparticle interactions as present in the BCS-BEC crossover [35]. Here k_B is the Boltzmann constant. In this limit, any physical quantity of the Fermi gas can be expanded as a series expansion in the fugacity z with corresponding expansion coefficients, i.e., the virial coefficients.

We employ the quantum virial expansion to calculate Tan's contact, following Ref. [13] where this approach was described and used to present the contact at unitarity and at $T = 0.5\,T_F$ for $-2 < (k_Fa_s)^{-1} < 0.5$. Using the same approach, we show results for the contact in the entire BCS-BEC crossover for $-1.5 < (k_Fa_s)^{-1} < 2.5$ and $0 < T/T_F < 1.5$ in Fig. 3(b) of Ref. [18] and for four different couplings $(k_Fa_s)^{-1}$ in Fig. 3. In Fig. 4 we further provide a map of the central fugacity z_0 of a harmonically trapped Fermi gas the BCS-BEC crossover.

To quickly rederive the calculation of the contact within the quantum virial expansion, we start from Tan's adiabatic

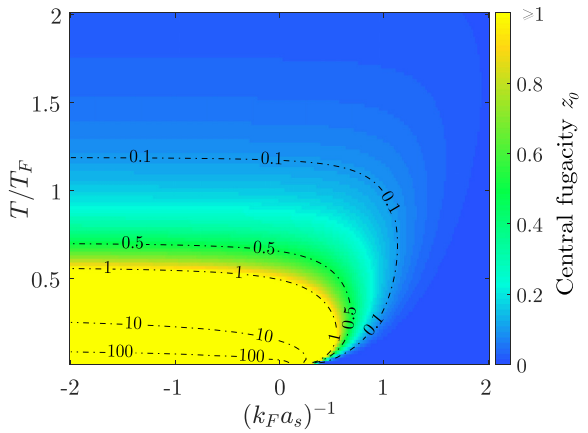

FIG. 4. Calculation of the fugacity z_0 in the center of a harmonically trapped Fermi gas in the BCS-BEC crossover. The calculation is based on the second-order quantum virial expansion. In regions where $z_0 \ll 1$ the expansion is expected to be valid.

sweep theorem for the grand canonical ensemble

$$\left(\frac{\partial \Omega_G}{\partial(1/a_s)}\right)_{T,V,\mu} = -\frac{\hbar^2 C V}{4\pi m}. \tag{11}$$

In the virial expansion, the grand canonical potential

$$\Omega_G = -2k_B T V/\lambda_{dB}^3 (z + b_2 z^2 + b_3 z^3 + \cdots) \tag{12}$$

is expanded as a series expansion in the fugacity $z = \exp(\mu/k_B T)$ where b_n are the virial coefficients, V is the volume, and λ_{dB} is the thermal de Broglie wavelength [23]. The virial coefficients are functions of λ_{dB} and the scattering length a_s. Using Eqs. (11) and (12) we find the homogeneous contact density

$$C_{QV} = \frac{16}{\pi^2 \lambda_{dB}^4}(c_2 z^2 + c_3 z^3 + \cdots) \tag{13}$$

for a given temperature T, chemical potential μ and scattering length where $c_n = \partial b_n/\partial(\lambda_{dB}/a_s)$. Using the local density approximation, one can calculate the total contact for the harmonically trapped Fermi gas with trap frequency ω by replacing the chemical potential μ with a local chemical potential $\mu(r) = \mu_0 - \frac{1}{2}m\omega^2 r^2$ and then integrating

$$\begin{aligned}\mathcal{I}_{QV} &= \int d^3r\, C(r) \\ &= \frac{16}{\pi^2 \lambda_{dB}^4}\int d^3r (c_2 z^2(r) + c_3 z^3(r) + \cdots) \\ &= \frac{16}{\pi^2 \lambda_{dB}}\left(\frac{k_B T}{\hbar\omega}\right)^3 \left[\frac{c_2}{2^{3/2}} z_0^2 + \frac{c_3}{3^{3/2}} z_0^3 + \cdots\right].\end{aligned} \tag{14}$$

Here, μ_0 is the chemical potential in the center of the trap and $z_0 = \exp(\mu_0/k_B T)$ is the corresponding fugacity. In a harmonically trapped Fermi gas, the chemical potential in the trap center is usually not known. Instead, the total atom number N is known, as it can be measured. Starting from the thermodynamic relation $n = -\frac{1}{V}\frac{\partial \Omega_G}{\partial \mu}$, and using again the local density approximation one finds

$$\begin{aligned}N &= \int d^3r\, n(r) = 2\left(\frac{k_B T}{\hbar\omega}\right)^3 \left[z_0 + \frac{b_2}{\sqrt{2}} z_0^2 + \frac{b_3}{\sqrt{3}} z_0^3 + \cdots\right] \\ &= 2\left(\frac{k_B T}{\hbar\omega}\right)^3 \left[z_0 + \frac{b_2^{(0)} + \Delta b_2}{\sqrt{2}} z_0^2 + \frac{b_3^{(0)} + \Delta b_3}{\sqrt{3}} z_0^3 + \cdots\right] \\ &= 2\left(\frac{k_B T}{\hbar\omega}\right)^3 \left[z_0 - \frac{z_0^2}{2^3} + \frac{z_0^3}{3^3} + \cdots + \frac{\Delta b_2}{\sqrt{2}} z_0^2 + \frac{\Delta b_3}{\sqrt{3}} z_0^3 + \cdots\right] \\ &= 2\left(\frac{k_B T}{\hbar\omega}\right)^3 \left[-\mathrm{Li}_3(-z_0) + \frac{\Delta b_2}{\sqrt{2}} z_0^2 + \frac{\Delta b_3}{\sqrt{3}} z_0^3 + \cdots\right],\end{aligned} \tag{15}$$

where we separated the virial coefficients in parts Δb_n that take into account the n-body interactions (e.g., scattering properties, bound states, etc.) and parts that account for quantum statistics $b_n^{(0)} = \frac{(-1)^{n+1}}{n^{5/2}}$. The infinite sum $z_0 - z_0^2/2^3 + z_0^3/3^3 + \cdots$ can be identified as the polylogarithm function $\mathrm{Li}_3(-z_0)$ of degree 3 and argument $-z_0$. The polylogarithm function is related to the integral of the Fermi-Dirac distribution function. The second-order virial coefficient is analytically known and reads [23,36]

$$b_2 = b_2^{(0)} + \Delta b_2 \tag{16}$$

$$= \frac{-1}{2^{5/2}} + \sqrt{2}\Theta(a_s) e^{\lambda_{dB}^2/2\pi a_s^2} - \frac{\sqrt{2}}{2}\mathrm{sgn}(a_s)\left(1 - \mathrm{erf}\left[\sqrt{\lambda_{dB}^2/2\pi a_s^2}\right]\right) e^{\lambda_{dB}^2/2\pi a_s^2}, \tag{17}$$

where $\Theta(\cdots)$ is the Heavyside step function, $\mathrm{sgn}(\cdots)$ is the sign function, and $\mathrm{erf}(\cdots)$ is the error function. By applying the virial expansion up to the second order, Eq. (15) can be solved numerically to determine μ_0 for a given atom number N, temperature T, scattering length a_s, and trap frequency ω. With the chemical potential, one can then calculate the contact of the trapped Fermi gas using Eq. (14). The result is shown in Fig. 4(b) of Ref. [18]. From the calculation of the central chemical potential μ_0, we also obtain the corresponding fugacity z_0 which is shown in Fig. 4. Its value indicates in which regimes the second-order virial expansion is expected to provide reliable results.

We also performed calculations of the contact with the third-order virial expansion. For this, we extracted b_3 from Ref. [37]. Above $(k_F a_s)^{-1} \approx 1.5$, the second- and third-order calculation give the same results for the contact. As also observed in Ref. [13], we find that the second- and third-order results at unitarity start to deviate from each other for temperatures lower than $\approx 0.5\, T_F$. Additional calculations for couplings $(k_F a_s)^{-1} = (-0.5, 0.5, 1)$ are shown in Fig. 3. When we go deeper into the BCS regime, the second- and third-order results start to deviate at temperatures even higher than $0.5\ T_F$. This is because in the BCS regime the fugacity $z_0 = \exp(\mu_0/k_B T)$ is not small anymore as the chemical potential μ_0 is positive and approaches the Fermi energy for $(k_F a_s)^{-1} \to -\infty$. As a result, the virial expansion loses its validity and the higher-order expansions do not converge.

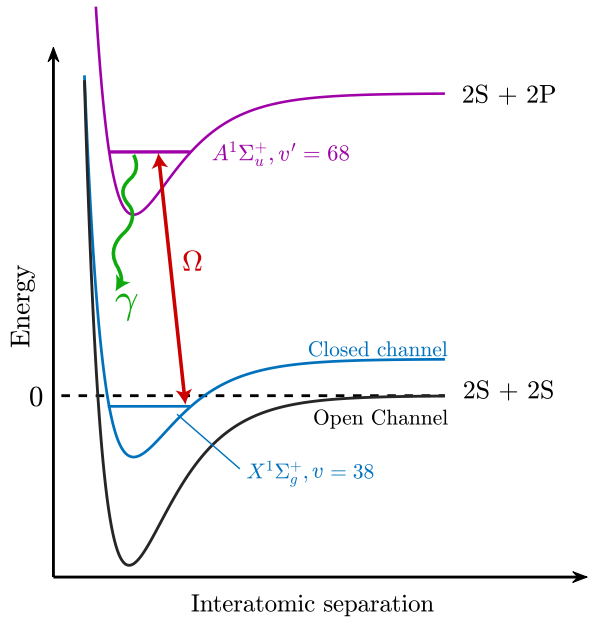

FIG. 5. Photoexcitation scheme for the measurements of Tan's contact via two-body losses, using the example of two colliding ground state ^{6}Li atoms in the lowest hyperfine levels $|F = 1/2, m_F = 1/2\rangle$ and $|F = 1/2, m_F = -1/2\rangle$. The magnetic field is close to 832.2 G where a broad Feshbach resonance is located. In the Feshbach resonance the scattering state of the atoms is coupled via the hyperfine interaction to the bare weakly bound molecular level $X^1\Sigma_g^+, v = 38$. This Feshbach resonance is essentially lossless. We induce two-body loss photoexciation using a laser at 673 nm, which couples the bare weakly bound molecular level $X^1\Sigma_g^+, v = 38$ state to the excited deeply-bound molecular state $A^1\Sigma_u^+ v' = 68$. The two states have a large Franck-Condon overlap of 0.077 [39]. The excited state has a lifetime γ. Ω is the Rabi frequency associated with this optical transition.

III. MEASUREMENT OF TAN'S CONTACT VIA PHOTOINDUCED TWO-BODY LOSS

As pointed out in Refs. [4,5] there is a very general and fundamental link between the total contact $\mathcal{I}$ and the two-body loss rate of a two-component Fermi gas

$$-\frac{dN}{dt} = \frac{-\hbar \mathrm{Im}[a]}{2\pi m|a|^2}\mathcal{I}, \tag{18}$$

where N is the total atom number, m is the atomic mass, and a is the scattering length. If a has a finite imaginary part, loss due to a two-body process is present. Thus, the total contact of the spin-balanced Fermi gas can be simply deduced from the induced two-body loss rate, as long as the scattering length is known. Note that relation (18) holds for collisional loss during s-wave collisions. A very similar relation was recently found for a collisional p-wave loss rate [14,15]. We now consider a special situation of two fermions colliding in an s-wave while they are subjected to a photoexcitation laser beam, see Fig. 5. Atomic collisions take place in the vicinity of a single, magnetically tunable Feshbach resonance. The Feshbach resonance comes about as a bare, closed-channel molecular bound state is coupled (via hyperfine interaction) and admixed to the scattering state of the colliding atoms. The Feshbach resonance is intrinsically lossless. Now, two-body loss is induced via resonant photoexcitation of the atom pair at close range to an electronically excited, short-lived molecular state with a lifetime $1/\gamma$. Photoexcitation takes place via the closed-channel bound state of the Feshbach resonance which is coupled to the excited molecular state with Rabi frequency Ω. For this system, the authors of Ref. [17] calculated the complex scattering length a and Eq. (18) becomes

$$-\frac{dN}{dt} = \frac{\hbar \mathcal{I}}{2\pi m a_{bg}} \frac{\Omega^2/(2\gamma W)}{[1 - a_{bg}/a_s]^{-2} + [\Omega^2/(2\gamma W)]^2}. \tag{19}$$

Here, a_s denotes the real-valued scattering length without the photoexcitation coupling, a_{bg} is the corresponding background scattering length, and W the width of the Feshbach resonance. In our experiments the resonance width is $W = -2\mu_B \times 262.3(3)\,\mathrm{G} = -2\pi\hbar \times 734(1)$ MHz, and $a_{bg} = -1582(1)\,a_0$ [38] where a_0 is the Bohr radius. The linewidth γ is $\gamma = 2\pi \times 12(1)$ MHz, as measured in our experiment [18]. The spectroscopic details of the excited and closed-channel molecular bound states, as well as the scattering state of our experiment can be found in Fig. 5 and the caption. For all practical purposes, the term $[\Omega^2/(2\gamma W)]^2$ in the denominator can be neglected in our experiments because we have $\Omega \lesssim 2\pi \times 1$ MHz. Even for Ω up to $2\pi \times 250$ MHz, the term $[\Omega^2/(2\gamma W)]^2$ is smaller than 10^{-3}.

According to Eq. (19) the contact $\mathcal{I}$ can be determined by measuring the atom loss rate $dN/dt \equiv \dot{N}$, the Rabi frequency Ω and the scattering length a_s in a given experimental run. To achieve a high precision for the value $\mathcal{I}$ at a particular $(k_F a_s)^{-1}$ and T/T_F, we need to precisely determine the Rabi frequency Ω, the atom number N, the trapping frequencies ω_{ax} and ω_r, as well as the scattering length a_s. [Note that $k_F = (2m/\hbar)^{1/2}(\omega_{ax}\omega_r^2 3N)^{1/6}$]. How this is achieved is described in the following sections.

A. Calibration of the Rabi frequency Ω

As a first step, we simplify Eq. (19), by omitting the term $[\Omega^2/(2\gamma W)]^2$ in the denominator, as it can be neglected in our experiments

$$-\dot{N} = \frac{\hbar \mathcal{I}}{2\pi m a_{bg}} \frac{\Omega^2/(2\gamma W)}{[1 - a_{bg}/a_s]^{-2}}. \tag{20}$$

Next, we make use of the fact that Ω is linked to the photoexcitation intensity I via the relation $\Omega^2 = k\,I$ where k is a constant. We use a calibration process to determine k and with it Ω. For this, we choose a convenient parameter setting for which the contact $\mathcal{I}$ is known. This parameter setting corresponds to a specific photoexcitation intensity I_{cal}, scattering length $a_{s,\mathrm{cal}}$ (via tuning of the magnetic field B), particle density, and temperature. Concretely, we chose the low-temperature BEC regime which has the advantage that the contact there is quite insensitive to temperature (see Fig. 3) and its value is $\mathcal{I}/Nk_F = 4\pi/(k_F a_s)$ [16]. We then measure the loss rate $\dot{N}_{\mathrm{cal}}$ at these parameters and this yields

$$k = -\dot{N}_{\mathrm{cal}} \frac{2\pi m a_{bg}}{\hbar \mathcal{I}_{\mathrm{cal}}} \frac{[1 - a_{bg}/a_{s,\mathrm{cal}}]^{-2}}{I_{\mathrm{cal}}/(2\gamma W)}. \tag{21}$$

Using Eq. (21) and the relation $\Omega^2 = k\,I$, Eq. (20) becomes

$$\dot{N} = \dot{N}_{\rm cal}\frac{\mathcal{I}}{\mathcal{I}_{\rm cal}}\frac{I}{I_{\rm cal}}\frac{[1-a_{bg}/a_{s,\rm cal}]^{-2}}{[1-a_{bg}/a_s]^{-2}}, \tag{22}$$

where the parameters m, γ, and W have dropped out as a consequence of the calibration.

B. Atom number calibration

For determining the atom number, we perform absorption imaging at high magnetic fields. For this purpose, we typically use a short laser pulse of $\tau = 10$ µs at an intensity of $I/I_S = 0.05$ to drive the quasiclosed transition to the $|2^2P_{3/2}; m_J = -3/2\rangle$ state with linewidth $\Gamma_a \approx 2\pi \times 5.87$ MHz [40], where $I_S = 2.54\,\mathrm{mW/cm^2}$ is the saturation intensity.

During the exposure with the imaging light, the atoms scatter photons. This accelerates them and leads to an increasing Doppler shift (see, e.g., Ref. [41]) which effectively lowers the cross section for absorption over time. To take this effect into account, we calibrated our imaging routine using a simple classical mechanical model. In this model, we consider the acceleration of the atoms

$$a = \frac{\hbar k\Gamma_a}{2m}\frac{I/I_S}{1+I/I_S+4(kv/\Gamma_a)^2}, \tag{23}$$

by scatting photons from the imaging beam with intensity I and wavelength $\lambda = 2\pi/k \approx 671$ nm [42]. Solving this differential equation yields the time-dependent atom velocity v and Doppler shift kv. From this, we can calculate a time-averaged cross section for absorption imaging which is lowered from the largest possible cross section by a factor $\langle 1 + I/I_s + 4(kv/\Gamma_a)^2\rangle_\tau$ due to the acquired Doppler shift and power broadening. We fit this model to our measured atom numbers with the intensity I and (real) atom number N as free parameters (see Fig. 6). This allows for extracting the accurate atom number at any given intensity and pulse duration. With this, we can determine atom numbers with a typical uncertainty of 5%, corresponding to an uncertainty in $k_F \propto N^{1/6}$ of 1%. We further tested this calibration using calculations of the atom cloud density distribution in the trap based on the equation of state at unitarity [28] and with a mean-field model in the low-temperature BEC regime which we describe in detail in the Supplementary Material of Ref. [43]. With this, we calculate the two-dimensional (2D) column density and one-dimensional (1D) line density for given total atom numbers, trapping frequencies, and temperatures and compare the calculated densities to the measured ones.

C. Trap frequency measurement and anharmonicities

While the trapping potential of the atoms in our experiment in axial direction is harmonic for all practical purposes, this is not quite the case in radial direction where a single-beam optical dipole trap provides confinement. Therefore, the radial-trapping potential has a Gaussian shape, thus increasingly deviating from a perfect harmonic potential with the distance from the trap center. The larger the atomic cloud size, the larger are the effects due to the anharmonicity [44]. Cloud sizes increase, e.g., due to stronger repulsive interparticle interactions and higher temperatures. Nevertheless,

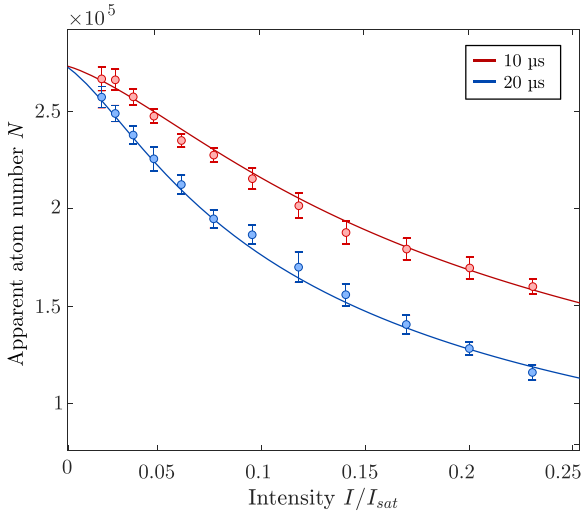

FIG. 6. Measured signal for the atom number as a function of the imaging light intensity for imaging pulse durations of 10 µs and 20 µs. The apparent atom number drops with higher intensity and imaging pulse duration due to an increasing Doppler shift that the atoms acquire while scattering photons. This effectively lowers the cross section for absorption and thus the measured atom numbers. In the limit of zero intensity, the real atom number is recovered.

it turns out that the anharmonicity effects are comparatively small in our experiments, so that we can neglect them to first order in our data analysis in Ref. [18]. This has the advantage that it keeps our data analysis simple. However, it induces a small systematic error on our results which nominally represent the normalized total contact $\mathcal{I}/Nk_F$ for a perfectly harmonically trapped gas. We estimated this systematic error as follows. We carried out calculations to describe the properties and behavior of the atomic gas in an anharmonic trap. For temperature $T \approx 0$ these calculations are based on the EOS [27] and for $T/T_F > 0.5$ they are based on the quantum virial expansion [13,23]. For our given anharmonic trap, temperature T, total atom number N, and scattering length a_s, we calculated the atomic density distribution, the effective trap frequency $\omega_{\rm eff}$, and the total contact using the local density approximation (LDA). The effective trap frequency $\omega_{\rm eff}$ is the frequency of the center-of-mass motion of the atom cloud in the anharmonic trap. It generally differs slightly from the trap frequency ω_r at the trap center [44]. Next, we follow our analysis protocol of Ref. [18] where we ignore anharmonicity and set $\omega_r = \omega_{\rm eff}$ to calculate E_F, T_F, k_F, and the normalized total contact $\mathcal{I}/Nk_F$. Finally, we compare this value for the normalized contact to the one for the perfect harmonic trap. We find, that they deviate by less than 0.3% (1.3%, 3.0%, 3.2%, 3.6%) at $T/T_F = 0$ (0.5, 1.0, 1.5, 2.0). These systematic deviations are smaller than the respective statistical uncertainties in our measurements which are typically ≈2% (4%, 6%, 9%, 12%) at $T/T_F = 0$ (0.5, 1.0, 1.5, 2.0). The statistical uncertainties decrease with decreasing temperature T, since in our experiments evaporative cooling leads to more stable atom numbers at lower temperatures.

For determining the trapping frequencies ω_{ax} and $\omega_{\rm eff}$, we perform either parametric heating by modulating the potential

of the optical dipole trap or we observe the center of mass motion of the atom cloud after an initial small displacement of a few micrometers. Both methods give consistent results with approximately 2% uncertainty for the parametric heating method and 3% uncertainty for the center of mass motion measurement.

D. Determination of scattering length a_s

To determine the scattering length a_s precisely, we we precisely measure the measured magnetic field at the location of the atoms. We then assign a scattering length to the measured magnetic field by using Ref. [38]. For measuring the magnetic fields precisely, we perform radio-frequency (RF) spectroscopy between the two lowest atomic hyperfine states. For this, we first use a short laser pulse to depopulate the $|F = 1/2, m_F = 1/2\rangle$ state. We then apply a 50 ms RF pulse and scan stepwise the RF frequency of ≈76.2 MHz to find resonant population transfer to this state from the still populated $|F = 1/2, m_F = -1/2\rangle$ state. Using the Breit-Rabi formula we are able to determine the magnetic field with an uncertainty <0.5 G. Together with the typical uncertainty in k_F of 1%, this results in an uncertainty of $(k_F a_s)^{-1} \approx 0.01$ in the investigated range of magnetic fields.

E. Thermometry

For determining the temperature of our atoms, we fit a second-order virial expansion of the density distribution to the outer wings of the atom cloud (see Refs. [43,45]). This works well even at low temperatures, as the local fugacity $z(\vec{r})$ in the outer wings is still a small parameter which makes the virial expansion applicable. With this method, we can determine the temperature with a typical precision of ≈0.02 T/T_F at small temperatures ($T < 0.5T_F$) and up to 0.05 T/T_F at high temperatures ($T \gtrsim 1\, T_F$).

IV. RELATED STUDIES

In this section, we present additional results and insights that we obtain from our measurements. More precisely, we compare the photoinduced atom decay measurements to predictions from Ref. [16] and measurements from Ref. [19] where a dependency of the decay law on the interaction regime was predicted and observed. We further extract the closed-channel fraction Z from our measurements and compare the results to various theoretical predictions [17,46–49] and experimental results [19,39].

A. Two-body decay laws in a Fermi gas

According to Eq. (19) the photoinduced two-body loss rate in the Fermi gas is proportional to the total contact $\mathcal{I}$ [17]. If the dependency of the contact on the atom number N is known, one can deduce the corresponding decay law for $N(t)$.

As calculated in Ref. [16] in the zero-temperature BCS limit, the integration of the homogeneous contact density over the trap volume yields the proportionality $\mathcal{I} \propto k_F^3 N$ and therefore $\dot{N}/N \propto N^{1/2}$. At unitarity one finds $\mathcal{I} \propto k_F N$ and hence $\dot{N}/N \propto N^{1/6}$. In the BEC limit $\mathcal{I} \propto N$ such that $\dot{N}/N = \text{const}$. Here $k_F = \sqrt{2mE_F}/\hbar$ is the Fermi momentum of the trapped gas, $E_F = k_B T_F = \hbar\bar{\omega}(3N)^{1/3}$ is the Fermi energy, and $\bar{\omega}$ is the geometric mean of the trapping frequencies. Thus, these differential equations have the form $\dot{N}/N \propto N^{1/b}$, where $b = 2$ in the BCS limit, $b = 6$ at unitarity and $b \to \infty$ in the BEC limit. Their solutions, i.e., the decay laws, are given by the power law

$$N(t) = N_0/(1 + \Gamma_0 t/b)^b, \tag{24}$$

with the initial decay rate Γ_0. We can now compare these predictions with our measurements.

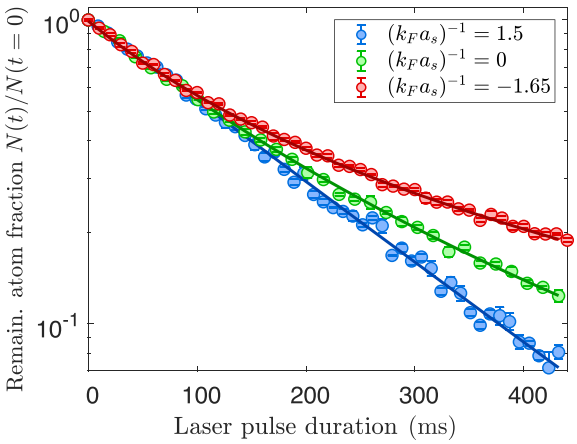

FIG. 7. Remaining atom fraction as a function of the photoexcitation laser pulse duration, taken from Ref. [18]. The measurements were carried out at magnetic fields of 753 G, 832 G, and 1078 G with the initial $(k_F a_s)^{-1} = 1.5,\ 0,\ -1.65$ corresponding to the BEC, unitarity and BCS regimes of the crossover. The initial temperatures were $T/T_F = 0.07,\ 0.05$, and 0.04, respectively. For a better comparison, the laser powers for the three data sets were manually adjusted so that their initial relative loss rates were the same (see Table I). The continuous red and green lines are fits according to Eq. (24), while the blue line is an exponential (i.e., $b = \infty$).

From our measurements shown in Fig. 7 we obtain the parameters b listed in Table I. We observe a deviation in the fit parameters b [see Eq. (3)] compared to the theoretical predictions. We attribute this deviation to an increase of the atom cloud temperature during the photoexcitation pulse, especially for longer times (>400 ms). Note, however, that we have not investigated this heating effect properly as after 400–500 ms thermometry based on the atom density distributions becomes increasingly difficult because the density and therefore the signal decreases. We find, however, that during the first 250 ms, the temperature stays rather constant within 5–10%. If we only include these data points, the fitted parameters tend towards the theoretical values. However, the uncertainty increases since we lower the number of data points for the fit. Our results for b are compatible with measurements of [19], who measured $b \approx 6$ at unitarity and $b = 1.78$ (1.43) in the BCS regime at 925 G (1000 G).

B. Closed-channel fraction

As discussed previously, in the vicinity of the Feshbach resonance the scattering wave function Ψ of an atom pair has a closed-channel admixture of the bare highest bound molecular state $X^1\Sigma_g^+(v = 38)$. It can be written as $\Psi = \sqrt{Z}\,\Psi_{\text{closed}} + \sqrt{1-Z}\,\Psi_{\text{open}}$ where Z is the so-called

TABLE I. Experimental parameters for the measurement data shown in Fig. 7. The values for couplings and temperatures are the initial values at $t = 0$.

Coupling $(k_F a_s)^{-1}$	Temperature	Photoex. laser power	Theo. param. b	Fit param. b	Fit param. b $t < 250$ ms
1.5	0.07 T_F	6 μW	∞	>20	>20
0	0.05 T_F	38 μW	6	3.9 ± 0.9	5.7 ± 3.1
−1.65	0.04 T_F	610 μW	2	1.6 ± 0.2	2.1 ± 0.5

closed-channel fraction. For a weak probe laser intensity ($\Omega^2 \ll \gamma W$) this quantity is directly linked to Tan's two-body contact via [16]

$$Z = \frac{\mathcal{I}}{Nk_F} \frac{\hbar k_F}{2\pi m a_{bg} W} \left[1 - \frac{a_{bg}}{a_s}\right]^2, \tag{25}$$

and has been experimentally and theoretically investigated by several groups [17,19,39,46–49]. It is, therefore, natural to compare all these data, see Fig. 8. However, since the closed-channel fraction is not a normalized quantity it can only be compared directly for measurements and calculations with similar parameters W, k_F, m, a_{bg}, a_s. Apart from some variations in the Fermi momentum k_F the parameters are indeed the same for the different data sets. Therefore, a quantitative comparison is approximately possible.

To calculate the magnetic field dependence of the closed channel fraction for any given Fermi momentum k_F we use the interpolation of our measurements of the total contact as presented in Fig. 2 in [18]. The measured quantity $\mathcal{I}/Nk_F$ only depends on $(k_F a_s)^{-1}$ to a good approximation. Thus, for a given Fermi momentum k_F and magnetic field B to which we assign a corresponding scattering length a_s, we can determine $\mathcal{I}/Nk_F$ from our interpolation. Using this result and Eq. (25), we can then calculate the closed-channel fraction Z. We use this procedure to calculate the blue lilac and green shaded areas in Fig. 8.

With the blue lilac shaded area we illustrate a lower and upper bound for the closed channel fraction deduced from our zero-temperature contact measurements where the atom number ranges from $4.8 \times 10^5 - 6.5 \times 10^5$ (corresponding to $k_F = 3.3 - 3.5\,\mu\text{m}^{-1}$). We further plot the closed channel fraction calculated for $k_F = 2.2$–$3.9\,\mu\text{m}^{-1}$. This allows for comparing our measurements to the ones presented in Ref. [39] where the Fermi momentum k_F ranges from 2.2 to $3.9\,\mu\text{m}^{-1}$ and to the calculation presented in [46] for $k_F = 2.2\,\mu\text{m}^{-1}$. The plot shows that up to this point there is still a large discrepancy between different measurements and theories on the BCS side of the Feshbach resonance. This highlights the importance of high precision measurements in this regime.

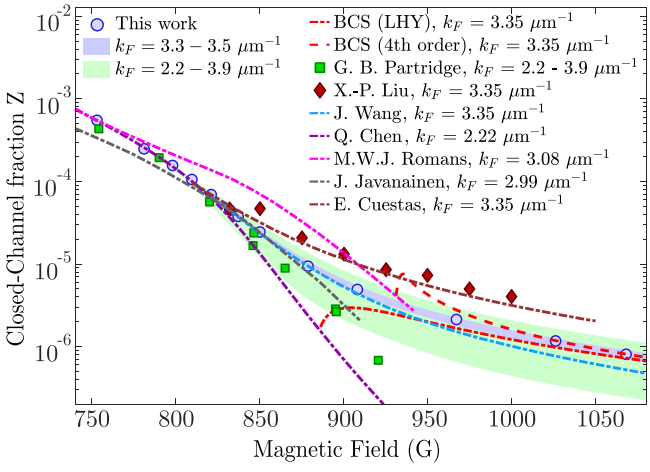

FIG. 8. Closed-channel fraction Z as a function of magnetic field, taken from various studies. Blue lilac circles are extracted from our measured contact data using Eq. (25). The blue lilac (green) shaded area is a calculation of the closed-channel fraction based on these results for the range of k_F from 3.2 to $3.5\,\mu\text{m}^{-1}$ (2.2 to $3.9\,\mu\text{m}^{-1}$). Data from other studies (calculations and measurements) have plot symbols as indicated by the legend. This includes photoexcitation measurements from Partridge *et al.* [39] and from Liu *et al.* [19], as well as calculations byWang *et al.* [17], Chen *et al.* [46], Romans *et al.* [47], Javanainen *et al.* [48], and Cuestas *et al.* [49]. We further show calculations based on the BCS ground-state energy expansions as in Fig. 2 of Ref. [18].

V. SUMMARY

In this companion paper, we present relevant background information on measuring Tan's contact in the BCS-BEC crossover with a photoexcitation method. After a brief overview over various previous approaches to determine the contact we identified areas in phase space of the strongly interacting Fermi gas where the contact is not known. We then lay out in detail the experimental method for measuring Tan's contact via photoexcitation, focusing on how to achieve contact measurements with high precision. Afterwards, we use our measurements to study and confirm various predicted decay laws in a Fermi gas due to two-body loss [16]. Finally, we extract the closed-channel fraction from our measurements and compare them to several previous theoretical and experimental studies. In the future it will be particularly worthwhile to employ the described photoexcitation method to measure Tan's contact in homogeneous Fermi gases, as this will allow for resolving details of Fermi gas properties which are washed out in our current experiments with trapped Fermi gases [17].

ACKNOWLEDGMENTS

We would like to acknowledge financial support by the German Research Foundation (DFG) through Grant No. 382572300, the Baden-Württemberg Foundation, and the Center for Integrated Quantum Science and Technology (IQST). We thank Hui Hu, Xia-Ji Liu, Jia Wang, Sascha Hoinka, and Chris Vale for valuable discussions. We thank

Frederik Koschnick and Wladimir Schoch for general assistance in the laboratory, and Markus Deiß, Dominik Dorer, Jinglun Li, and Wolfgang Limmer for discussions and support.

[1] S. Tan, Energetics of a strongly correlated Fermi gas, Ann. Phys. (NY) **323**, 2952 (2008).

[2] S. Tan, Large momentum part of a strongly correlated Fermi gas, Ann. Phys. (NY) **323**, 2971 (2008).

[3] S. Tan, Generalized virial theorem and pressure relation for a strongly correlated Fermi gas, Ann. Phys. (NY) **323**, 2987 (2008).

[4] E. Braaten, Universal relations for fermions with large scattering length, Lect. Notes Phys. **836**, 193 (2012).

[5] E. Braaten, L. Platter, Exact relations for a strongly-interacting Fermi gas from the operator product expansion, Phys. Rev. Lett. **100**, 205301 (2008).

[6] J. T. Stewart, J. P. Gaebler, T. E. Drake, and D. S. Jin, Verification of universal relations in a strongly interacting Fermi gas, Phys. Rev. Lett. **104**, 235301 (2010).

[7] Y. Sagi, T. E. Drake, R. Paudel, and D. S. Jin, Measurement of the homogeneous contact of a unitary Fermi gas, Phys. Rev. Lett. **109**, 220402 (2012).

[8] B. Mukherjee, P. B. Patel, Z. Yan, R. J. Fletcher, J. Struck, and M. W. Zwierlein, Spectral response and contact of the unitary Fermi gas, Phys. Rev. Lett. **122**, 203402 (2019).

[9] C. Shkedrov, M. Menashes, G. Ness, A. Vainbaum, E. Altman, and Y. Sagi, Absence of heating in a uniform Fermi gas created by periodic driving, Phys. Rev. X **12**, 011041 (2022).

[10] S. Hoinka, M. Lingham, K. Fenech, H. Hu, C. J. Vale, J. E. Drut, and S. Gandolfi, Precise determination of the structure factor and contact in a unitary Fermi gas, Phys. Rev. Lett. **110**, 055305 (2013).

[11] S. Laurent, M. Pierce, M. Delehaye, T. Yefsah, F. Chevy, and C. Salomon, Connecting few-body inelastic decay to quantum correlations in a many-body system: A weakly coupled impurity in a resonant Fermi gas, Phys. Rev. Lett. **118**, 103403 (2017).

[12] F. Palestini, A. Perali, P. Pieri, and G. C. Strinati, Temperature and coupling dependence of the universal contact intensity for an ultracold Fermi gas, Phys. Rev. A **82**, 021605(R) (2010).

[13] H. Hu, X.-J. Liu, and P. D. Drummond, Universal contact of strongly interacting fermions at finite temperatures, New J. Phys. **13**, 035007 (2011).

[14] X.-Y. Gao, D. Blume, and Y. Yan, Temperature-dependent contact of weakly interacting single-component Fermi gases and loss rate of degenerate polar molecules, Phys. Rev. Lett. **131**, 043401 (2023).

[15] M. He, C. Lv, H.-Q. Lin, and Q. Zhou, Universal relations for ultracold reactive molecules, Sci. Adv. **6**, eabd4699 (2020).

[16] F. Werner, L. Tarruell, and Y. Castin, Number of closed-channel molecules in the BEC-BCS crossover, Eur. Phys. J. B **68**, 401 (2009).

[17] J. Wang, X.-J. Liu, and H. Hu, Photoexcitation measurement of Tan's contact for a strongly interacting Fermi gas, Phys. Rev. A **104**, 063309 (2021).

[18] M. Jäger, and J. Hecker Denschlag, companion paper, Precise photoexcitation measurement of Tan's contact in the entire BCS-BEC crossover, Phys. Rev. Lett. **132**, 263401 (2024).

[19] X.-P. Liu, X.-C. Yao, H.-Z. Chen, X.-Q. Wang, Y.-X. Wang, Y.-A. Chen, Q. Chen, K. Levin, and J.-W. Pan, Observation of the density dependence of the closed-channel fraction of a ^{6}Li superfluid, Nat. Sci. Rev. **9**, nwab226 (2022).

[20] Y. Ohashi, H. Tajima, and P. van Wyk, BCS–BEC crossover in cold atomic and in nuclear systems, Prog. Part. Nucl. Phys. **111**, 103739 (2020).

[21] S. Giorgini, L. P. Pitaevskii, and S. Stringari, Theory of ultracold atomic Fermi gases, Rev. Mod. Phys. **80**, 1215 (2008).

[22] C. A. Regal, and D. S. Jin, Experimental realization of the BCS-BEC crossover with a Fermi gas of atoms, Adv. At. Mol. Opt. Phys. **54**, 1 (2007).

[23] X.-J. Liu, Virial expansion for a strongly correlated Fermi system and its application to ultracold atomic Fermi gases, Phys. Rep. **524**, 37 (2013).

[24] T. Enss, R. Haussmann, and W. Zwerger, Viscosity and scale invariance in the unitary Fermi gas, Ann. Phys. **326**, 770 (2011).

[25] O. Goulko and M. Wingate, Numerical study of the unitary Fermi gas across the superfluid transition, Phys. Rev. A **93**, 053604 (2016).

[26] R. Rossi, T. Ohgoe, E. Kozik, N. Prokof'ev, B. Svistunov, K. Van Houcke, and F. Werner, Contact and momentum distribution of the unitary Fermi gas, Phys. Rev. Lett. **121**, 130406 (2018).

[27] N. Navon, S. Nascimbène, F. Chevy, and C. Salomon, The equation of state of a low-temperature Fermi gas with tunable interactions, Science **328**, 729 (2010).

[28] M. J. H. Ku, A. T. Sommer, L. W. Cheuk, and M. W. Zwierlein, Revealing the superfluid Lambda transition in the universal thermodynamics of a unitary Fermi gas, Science **335**, 563 (2012).

[29] G. A. Baker, Jr., Neutron matter model, Phys. Rev. C **60**, 054311 (1999).

[30] T. D. Lee, K. Huang, and C. N. Yang, Eigenvalues and eigenfunctions of a Bose system of hard spheres and its low-temperature properties, Phys. Rev. **106**, 1135 (1957).

[31] X. Li, X. Luo, S. Wang, K. Xie, X.-P. Liu, H. Hu, Y.-A. Chen, X.-C. Yao, and J.-W. Pan, Second sound attenuation near quantum criticality, Science **375**, 528 (2022).

[32] D. S. Petrov, C. Salomon, and G. V. Shlyapnikov, Weakly bound dimers of fermionic atoms, Phys. Rev. Lett. **93**, 090404 (2004).

[33] P. S. Julienne and J. M. Hutson, Contrasting the wide Feshbach resonances in ^{6}Li and ^{7}Li, Phys. Rev. A **89**, 052715 (2014).

[34] B. Gao, Binding energy and scattering length for diatomic systems, J. Phys. B: At. Mol. Opt. Phys. **37**, 4273 (2004).

[35] T. L. Ho and E. J. Mueller, High temperature expansion applied to fermions near Feshbach resonance, Phys. Rev. Lett. **92**, 160404 (2004).

[36] E. Beth and G. E. Uhlenbeck, The quantum theory of the non-ideal gas. II. Behaviour at low temperatures, Physica **4**, 915 (1937).

[37] X. Leyronas, Virial expansion with Feynman diagrams, Phys. Rev. A **84**, 053633 (2011).

[38] G. Zürn, T. Lompe, A. N. Wenz, S. Jochim, P. S. Julienne, and J. M. Hutson, Precise characterization of ^{6}Li Feshbach resonances using trap-sideband-resolved RF spectroscopy of weakly bound molecules, Phys. Rev. Lett. **110**, 135301 (2013).

[39] G. B. Partridge, K. E. Strecker, R. I. Kamar, M. W. Jack, and R. G. Hulet, Molecular probe of pairing in the BEC-BCS crossover, Phys. Rev. Lett. **95**, 020404 (2005).

[40] W. I. McAlexander, E. R. I. Abraham, and R. G. Hulet, Radiative lifetime of the 2*P* state of lithium, Phys. Rev. A **54**, R5(R) (1996).

[41] K. Hueck, N. Luick, L. Sobirey, J. Siegl, T. Lompe, H. Moritz, L. W. Clark, and C. Chin, Calibrating high intensity absorption imaging of ultracold atoms, Opt. Express **25**, 8670 (2017).

[42] C. J. Foot, *Atomic Physics* (Oxford University Press, New York, 2005), Vol. 7.

[43] D. K. Hoffmann, V. P. Singh, T. Paintner, M. Jäger, W. Limmer, L. Mathey, and J. Hecker Denschlag, Second sound in the crossover from the Bose-Einstein condensate to the Bardeen-Cooper-Schrieffer superfluid, Nat. Commun. **12**, 7074 (2021).

[44] A. Altmeyer, S. Riedl, C. Kohstall, M. J. Wright, R. Geursen, M. Bartenstein, C. Chin, J. Hecker Denschlag, and R. Grimm, Precision measurements of collective oscillations in the BEC-BCS crossover, Phys. Rev. Lett. **98**, 040401 (2007).

[45] T. Paintner, D. K. Hoffmann, M. Jäger, W. Limmer, W. Schoch, B. Deissler, M. Pini, P. Pieri, G. C. Strinati, C. Chin, and J. Hecker Denschlag, Pair fraction in a finite-temperature Fermi gas on the BEC side of the BCS-BEC crossover, Phys. Rev. A **99**, 053617 (2019).

[46] Q. Chen and K. Levin, Population of closed-channel molecules in trapped Fermi gases with broad Feshbach resonances, Phys. Rev. Lett. **95**, 260406 (2005).

[47] M. W. J. Romans and H. T. C. Stoof, Dressed Feshbach molecules in the BEC-BCS crossover, Phys. Rev. Lett. **95**, 260407 (2005).

[48] J. Javanainen, M. Koštrun, M. Mackie, and A. Carmichael, Simple mean-field theory for a zero-temperature fermionic gas at a Feshbach resonance, Phys. Rev. Lett. **95**, 110408 (2005).

[49] E. Cuestas and A. P. Majtey, A generalized molecule approach capturing the Feshbach-induced pairing physics in the BEC-BCS crossover, J. Phys.: Condens. Matter **33**, 255601 (2021).